UCLA
UCLA Previously Published Works

Title

Warmth elevating the depths: shallower voids with warm dark matter

Permalink

https://escholarship.org/uc/item/1880z3gp

Journal

Monthly Notices of the Royal Astronomical Society, 451(4)

ISSN

0035-8711

Authors

Yang, Lin F
Neyrinck, Mark C
Aragón-Calvo, Miguel A
et al.

Publication Date

2015-08-21

DOI

10.1093/mnras/stv1087

Peer reviewed

Warmth elevating the depths: shallower voids with warm dark matter

Lin F. Yang,[1][*] Mark C. Neyrinck,[1] Miguel A. Aragón-Calvo,[2] Bridget Falck[3]
and Joseph Silk[1,4,5]

[1]*Department of Physics & Astronomy, The Johns Hopkins University, 3400 N Charles Street, Baltimore, MD 21218, USA*
[2]*Department of Physics and Astronomy, University of California, Riverside, CA 92521, USA*
[3]*Institute of Cosmology and Gravitation, University of Portsmouth, Dennis Sciama Building, Burnaby Rd, Portsmouth PO1 3FX, UK*
[4]*Institut d'Astrophysique de Paris – 98 bis boulevard Arago, F-75014 Paris, France*
[5]*Beecroft Institute of Particle Astrophysics and Cosmology, Department of Physics, University of Oxford, Denys Wilkinson Building, 1 Keble Road, Oxford OX1 3RH, UK*

ABSTRACT

Warm dark matter (WDM) has been proposed as an alternative to cold dark matter (CDM), to resolve issues such as the apparent lack of satellites around the Milky Way. Even if WDM is not the answer to observational issues, it is essential to constrain the nature of the dark matter. The effect of WDM on haloes has been extensively studied, but the small-scale initial smoothing in WDM also affects the present-day cosmic web and voids. It suppresses the cosmic 'sub-web' inside voids, and the formation of both void haloes and subvoids. In *N*-body simulations run with different assumed WDM masses, we identify voids with the ZOBOV algorithm, and cosmic-web components with the ORIGAMI algorithm. As dark-matter warmth increases (i.e. particle mass decreases), void density minima grow shallower, while void edges change little. Also, the number of subvoids decreases. The density field in voids is particularly insensitive to baryonic physics, so if void density profiles and minima could be measured observationally, they would offer a valuable probe of the nature of dark matter. Furthermore, filaments and walls become cleaner, as the substructures in between have been smoothed out; this leads to a clear, mid-range peak in the density PDF.

Key words: cosmology: theory – dark matter.

1 INTRODUCTION

There is overwhelming evidence (e.g. Frenk & White 2012) for the existence of dark matter (DM), whose nature is still unknown. Although many direct or indirect detection experiments (e.g. Agnese et al. 2013; Aprile 2013; Ackermann et al. 2014; Akerib et al. 2014) have occurred and are ongoing, no conclusive result has been reported.

It has been long known (Peebles 1980; Bertone, Hooper & Silk 2005) that the matter of the universe is dominated by DM. For structure formation, the velocity distribution of DM particles plays an important role. In the standard Λ cold dark matter (ΛCDM) model, the DM is assumed to be entirely cold from the standpoint of structure formation. The velocity dispersion is negligible at the era of matter-radiation equality (t_{eq}), and structure formation proceeds in a bottom-up fashion. Smaller structures form at first, then larger ones. This model has only a few parameters, that have been determined with high precision. However, several problems remain unsolved on sub-galactic scales. First, the missing satellite problem: simple arguments applied to CDM-only simulations imply that thousands

or hundreds of dwarf galaxies are expected in the Local Group and halo of the Milky Way, however only of the order 10 of them were found (Mateo 1998; Moore et al. 1999a). Secondly, CDM predicts concentrated density profiles in the central region, e.g. r^{-1} in the NFW (Navarro, Frenk & White 1997) profile, whereas many studies of galaxy rotation curves have concluded that the density approaches a constant in the core (Moore et al. 1999b; Ghigna et al. 2000). Thirdly, the number of dwarf galaxies expected in local voids may be less than a CDM model would predict (Peebles 2001).

Although better modelling of hydrodynamics and feedback processes may solve these problems (e.g. Hoeft et al. 2006), changing the DM itself could also help resolve some of the issues. Warm dark matter (WDM) has been an attractive alternative since the 1980s (e.g. Schaeffer & Silk 1988). Recently, the WDM model has received some interest since it can reproduce all the successful CDM results on large scales, but also solve some small-scale issues. The key feature separating WDM from CDM models is the lack of initial small-scale fluctuations. The WDM has slightly larger velocity dispersion at t_{eq}, giving a smoothing of initial fluctuations at a free-streaming length determined by the WDM particle mass. From particle physics, the originally favoured WDM candidate was a gravitino (e.g. Moroi, Murayama & Yamaguchi 1993); more recently, a sterile neutrino (Boyarsky et al. 2009) has seen attention.

[*] E-mail: lyang36@jhu.edu

Both theoretical and numerical studies (e.g. Bode, Ostriker & Turok 2001) have explored WDM models, and observational constraints have been put on the mass of WDM particles. For example, Viel et al. (2013) give a lower limit of $m_X = 3.3$ keV from Lyman α forest data. Other independent studies (e.g. Miranda & Macciò 2007) also give consistent limits.

While previous studies on WDM mainly focused on the formation of haloes or other dense structures, there has been some work investigating the cosmic web itself. Schneider et al. (2012) studied voids in a WDM scenario, but focus on the halo population within them, finding that voids are emptier (of haloes and substructure) in WDM. Below, we study the dark-matter density itself, which follows the opposite trend, growing in density in WDM. Reed et al. (2014) also studied the large-scale-structure traced out by galaxies in a WDM scenario, including a study of galaxy environment. They found that WDM makes very little difference in the usual observables of the galaxy population, when using subhalo abundance matching to identify galaxies. That is, they found that the subhaloes in the DM, above a mass threshold where halo formation is not substantially disrupted from the loss of power in WDM, are arranged in nearly the same way in WDM and CDM. Hydrodynamic simulations that include star formation indicate that stars may form in filaments instead of haloes if the DM is quite warm (Gao & Theuns 2007; Gao, Theuns & Springel 2014), an issue related to the low 'complexity' of dark-matter halo structure in WDM (Neyrinck 2014b).

Voids are large underdense regions, occupying the majority of the volume of the Universe, and are valuable cosmological probes. For example, via the Alcock–Paczynski test, voids serve as a powerful tool to detect the expansion history of the universe (e.g. Ryden 1995; Lavaux & Wandelt 2012). Clampitt, Cai & Li (2013), Cai, Padilla & Li (2014) and Li, Zhao & Koyama (2012) have also proposed voids as a probe of modified gravity. The abundance of voids may be sensitive to initial conditions (Kamionkowski, Verde & Jimenez 2009), hence voids may serve as probes of the early universe. Previous work has also looked at voids in the context of WDM. Tikhonov et al. (2009) measured the abundance of mini-voids, which become scarcer in a WDM model. Recently, Clampitt & Jain (2014) detected void lensing at a significance of 13σ, raising hopes for void density-profile measurements using lensing. The few-parameter 'universal' form for void density profiles that Hamaus, Sutter & Wandelt (2014) found will likely help in extracting cosmological information from voids.

In this paper, we study how properties of voids in the cosmic web change in a WDM scenario, with different initial power-spectrum attenuations corresponding to different WDM masses. We analyse these simulations with the ZOBOV void-finder (Neyrinck 2008) and the ORIGAMI (Falck, Neyrinck & Szalay 2012), filament, wall and halo classifier. The paper is laid out as follows. In Section 2, we introduce our WDM N-body simulations. In Section 3, we analyse the full cosmic web of DM in a WDM scenario. In Section 4, we introduce our void detection methods and shows the void statistical properties. In Section 5, we show the distinct features of void density profiles for different DM settings. We give our conclusions and discussion in Section 6.

2 SIMULATIONS

We simulate both CDM and WDM using the GADGET-2 (Springel 2005) code. We use the Zel'dovich approximation (Zel'dovich 1970) to impart initial displacements and velocities at redshift $z = 127$ to particles on the initial lattice of 512^3 particles in a

periodic box of size 100 h^{-1} Mpc. The initial power spectrum was generated with the CAMB code (Lewis, Challinor & Lasenby 2000), using vanilla Λ(C)DM cosmological parameters ($h = 0.7$, $\Omega_M = 0.3$, $\Omega_\Lambda = 0.7$, $\Omega_b = 0.045$, $\sigma_8 = 0.83$, $n_s = 0.96$).

To incorporate the effect of a thermally produced relic WDM particle, we apply the following fitting formula to the transfer functions (Bode et al. 2001),

$$T_{WDM} = T_{CDM}(k)[1 + (\alpha k)^2]^{-5.0}, \tag{1}$$

where the cutoff scale

$$\alpha = 0.05 \left(\frac{\Omega_m}{0.4}\right)^{0.15} \left(\frac{h}{0.65}\right)^{1.3} \left(\frac{m_{dm}}{1 keV}\right)^{-1.15} \left(\frac{1.5}{g_X}\right)^{0.29} h^{-1} Mpc. \tag{2}$$

Here, m_{dm} is the mass of the WDM particle (or the effective sterile neutrino); g_X is the number of degrees of freedom that the WDM particle contributes to the number density (in our case, 3/2). In our set of simulations, we applied $\alpha = 0$, 0.05, 0.1 and 0.2 h^{-1} Mpc, corresponding first to CDM, and then to WDM particle masses 1.4, 0.8 and 0.4 keV. Note that these masses of sterile neutrinos are disfavoured by Lyman α forest data (Viel et al. 2013), but we adopt them to show the effect of WDM without great computational cost.

Only in the most extreme case of 0.2 h^{-1} Mpc is α comparable to the interparticle separation. The reason that differences show up even when α is below this scale is the broad shape of the attenuation described in equation (2). Bode et al. (2001) define a perhaps more meaningful 'half-mode' scale radius R_s, via $T(\pi/R_s) = 1/2$; this quantity is $\sim 6\alpha$. We hold σ_8 fixed in the linear power spectrum. This changes the large-scale amplitude, but very slightly since the smoothing kernel acts on scales well below 8 h^{-1} Mpc.

We emphasize that the differences between CDM and the WDM models would increase with the mass resolution, because even with '$\alpha = 0$', there is a cutoff in the initial power spectrum from the interparticle spacing of 0.2 h^{-1} Mpc. To illustrate this, we show in Fig. 1 the expected minimum density, as a function of resolution, in a 100 h^{-1} Mpc box, for CDM and WDM models. We estimate this as follows. As shown below in Fig. 3, the spherical-collapse limit (Bernardeau 1994; Protogeros & Scherrer 1997; Neyrinck 2013)

$$\delta_{sc} + 1 = [1 - (2/3)\delta_{lin}]^{-3/2} \tag{3}$$

accurately gives the transformation from linear to non-linear density on the low-density tail. The lowest linear-theory density in the box will be the expected minimum value of a Gaussian in a sample of $N_{cells} = [(100 \ h^{-1} \ Mpc)/c]^3$ cells, where c is the cell size. This is

$$\delta_{lin}^{min} = -\sigma(c)\sqrt{2} erf^{-1}(2/N_{cells}), \tag{4}$$

where $\sigma(c)$ is the linear-theory density dispersion in cells of size c. (We approximate $\sigma(c)$ with a spherical top-hat kernel of the same volume as a cubic cell.) As c decreases, the WDM and CDM curves diverge, because $\sigma(c)$ increases in CDM, but not in WDM. The WDM curves do continue to decrease slightly, however, because the number of cells increases.

We have not included the thermal velocity kicks to the individual particles to our simulation, for two reasons. First, particles in the simulation are averages over a statistical ensemble of particles, so it is unclear how to implement the thermal velocity in the initial conditions. Also, this thermal velocity would be negligible for our results. For the α values we use, the rms velocity distribution is of order 1 km s^{-1} (Angulo, Hahn & Abel 2013), while typical velocities of particles inside a void are of order 50 km s^{-1} at radius around $0.5r_v$ (Hamaus, Sutter & Wandelt 2014). We do not employ a method to
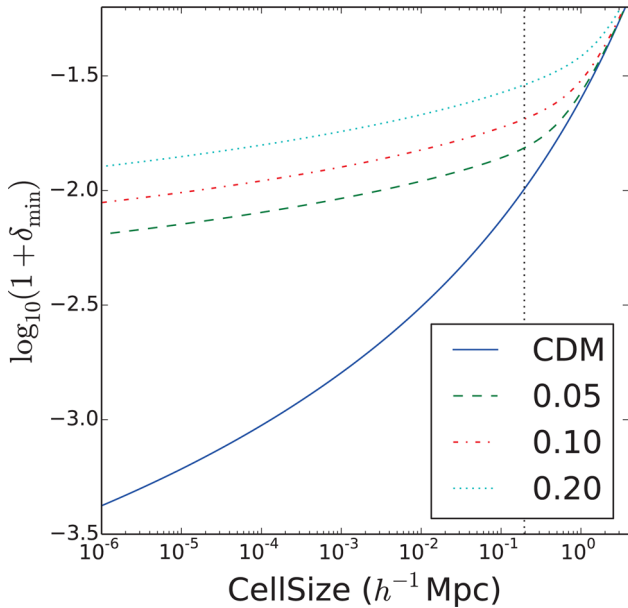
Figure 1. The minimum density expected in a $(100\ h^{-1}\ \mathrm{Mpc})^3$ volume, as a function of simulation resolution. The four curves show the four cases investigated below: the WDM cut-off scale $\alpha = 0$ (CDM), 0.05, 0.1, and $0.2\ h^{-1}$ Mpc. The cell size is the initial comoving interparticle separation. A dashed line shows the cell size for the resolution used in the simulations used in this work.

prevent spurious fragmentation in filaments (Wang & White 2007), because we focus on voids instead of haloes. Spurious fragmentation should only upscatter particles in morphological type, i.e. turning wall particles into filament or halo particles, and filament particles into halo particles. This artificial fragmentation happens in the presence of anisotropy, but should not happen in voids, where even initially anisotropic volume elements grow nearly isotropic with time (Icke 1984).

3 THE COSMIC WEB IN A WDM SCENARIO

Fig. 2 shows a slice of an LTFE (Lagrangian Tessellation Field Estimator; Abel, Hahn & Kaehler 2012) density field of the simulation. This estimator makes use of the fact that, under only gravity, the 3D manifold of DM particles evolve in phase space without tearing, conserve phase space volume and preserve connectivity of nearby points. Hence, the sheets (or streams) formed by the initial grids are assumed to remain at constant mass in the final snapshot. Using the initial grid position (or the Lagrangian coordinates) of each particle, the density of each stream could be calculated. We implemented an OpenGL code of LTFE to estimate the density field in a time efficient way. The differences of density fields are clear: small-scale structures are smoothed out in the WDM simulations.

Fig. 3 shows mass-weighted 1-point PDFs (probability density functions) at $z = 0$ from the simulations, for each α. We measured the density at each particle using the Voronoi Tessellation Field Estimator (VTFE; Schaap & van de Weygaert 2000; van de Weygaert & Schaap 2009). In the VTFE, each particle occupies a Voronoi cell, a locus of space closer to that particle than any other particle. The density $\delta_{\mathrm{VTFE}} + 1 = \langle V \rangle / V$ at a particle is set by the volume V of its cell. This density measure is in a sense Lagrangian, but only strictly so without multistreaming.

At $\alpha = 0$, this mass-weighted PDF shows two clear peaks, noted by Neyrinck (2008). It was already clear that the higher-density
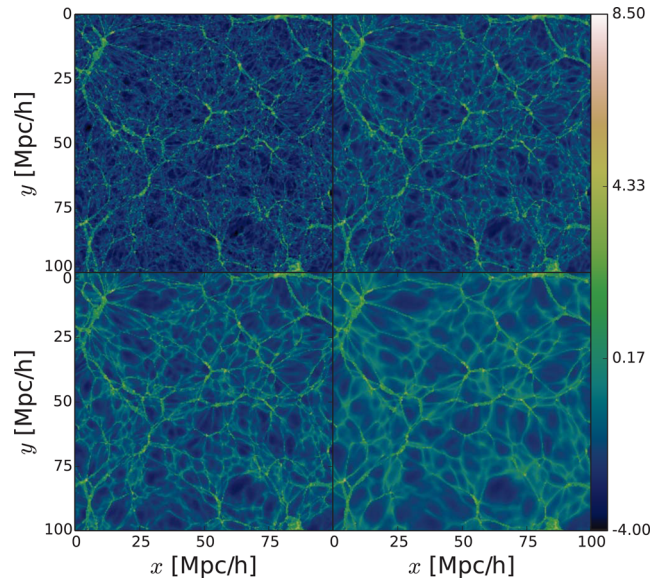

Figure 2. LTFE density field slices, showing $\ln(1 + \delta)$. From top left to bottom right: CDM, WDM with $\alpha = 0.05\ h^{-1}$ Mpc, WDM with $\alpha = 0.1\ h^{-1}$ Mpc and WDM with $\alpha = 0.2\ h^{-1}$ Mpc.

peak, a roughly lognormal peak at $\delta \approx e^{6-7} \approx 1000$, comes from halo particles. Falck et al. (2012) firmly established this halo origin by classifying particles with the ORIGAMI algorithm, into void (single-stream), wall, filament, and halo morphologies. This algorithm counts the number of orthogonal axes along which a particle has been crossed by any other particle, comparing the initial and final conditions.

For $\alpha = 0$, the lumpy shape of the total PDF at low densities already suggests that there may be more than two components. As α increases, however, an intermediate wall+filament peak becomes unmistakable: the visual impression from the density-field maps that a greater fraction of the matter is in walls and filaments is obvious in the total PDF as well. Again, the ORIGAMI classification confirms this picture. As the WDM mass increases, particles move from low to high densities and morphologies, through the different peaks. A similar effect happens as a function of simulation resolution in CDM: at higher resolution (smaller interparticle separation), the fraction of halo particles increases and fraction of void particles decreases. However, no obvious intermediate wall+filament peak appears in the total CDM PDF (Falck & Neyrinck 2015). The fractions of particles in walls and filaments remain about constant, with most of the change in particle morphologies appearing in the void and halo peaks. There is a change in the mean log-densities of the wall and filament peaks, however; while a substantial fraction of wall particles have $\delta < 0$ with CDM, note that only the end of the wall tail has $\delta < 0$ when $\alpha = 0.2$.

We note that this complicated PDF shape is likely poorly constrained by its first few moments, certainly not the moments of the overdensity δ, and likely not even the log-density $\ln(\delta + 1)$, the x-axis of the plot (e.g. Carron 2011; Carron & Neyrinck 2012). This is a case in which analysing the instead of the first few moments would be prudent (e.g. Hill et al. 2014; Neyrinck 2014c).

Also plotted is a successful analytic expression for the distribution of void-particle densities (Protogeros & Scherrer 1997; Neyrinck 2013), derived from a low-Ω_M limit (especially valid for voids) to
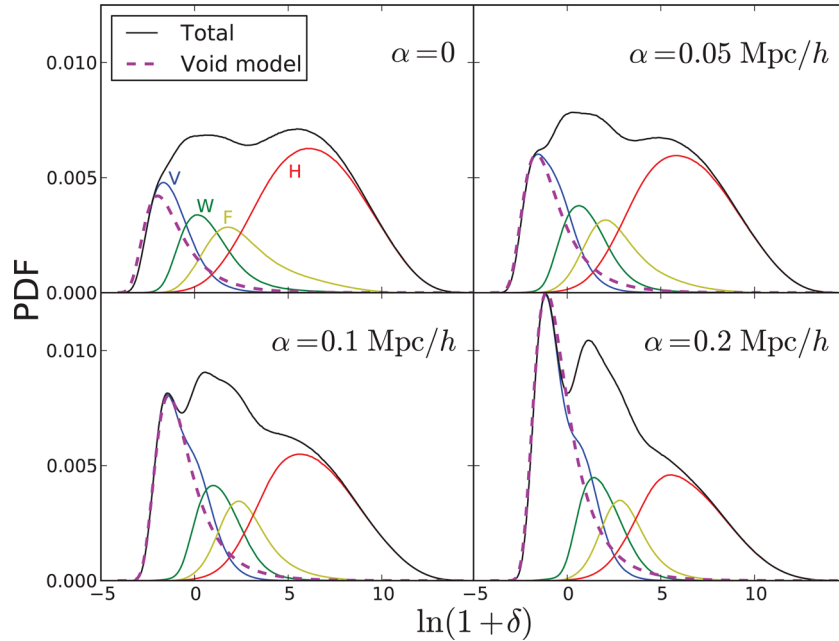
Figure 3. PDFs of particle densities for the four simulations. A distinctive peak arises from filament and wall particles at middling densities in a WDM scenario. The *V*, *W*, *F*, and *H* curves add up to the total: they separate out void, filament, wall, and halo particles, with crossings along 0, 1, 2, and 3 orthogonal axes. $\alpha = 0$ corresponds to CDM; as α increases, the WDM becomes warmer. In this mass-weighted PDF, each particle (Lagrangian element of initial spacing $0.2\ h^{-1}$ Mpc) enters once. The dashed magenta curve shows the expression in equation (5).

the evolution of an average mass element (Bernardeau 1994). The PDF of the log-density $A \equiv \ln(1 + \delta)$ is

$$P(A) = f_{\text{void}} \frac{\exp\left[-\frac{2}{3}A - \frac{(3/2)^2}{2\sigma^2} \left(e^{-(2/3)A} - 1 \right)^2 \right]}{\sqrt{2\pi\sigma^2}}, \quad (5)$$

where σ^2 is the linearly-extrapolated initial variance in cells of size the initial interparticle spacing. f_{void} is the fraction of void, single-stream particles, as measured by ORIGAMI. σ^2 is the variance in spheres of radius $L/N/(4\pi/3)^{1/3}$ (where $L = 100\ h^{-1}$ Mpc is the box size, and $N = 512$) as calculated from a CAMB linear power spectrum at $z = 0$, truncating the power spectrum to zero at $k > \pi/(L/N)$.

In Figs 4 and 5, Lagrangian-space density maps show where these various density regimes appear in the cosmic web. Here, each pixel represents a particle, arranged on its initial lattice. In Fig. 5, wart-like blobs within black contours are haloes; these contract substantially in the mapping to comoving $z = 0$ Eulerian space. The regions within white contours are void regions, which expand in comoving coordinates and come to fill most of the space; see Falck et al. (2012) for more detail and an alternative plotting method.

Regarding the topology of the void region, an increase in α decreases the amount of stream-crossing. At high α, even though filaments and walls become more evident visually in the density field, the decreased stream-crossing makes the percolation of the void region even more obvious than in CDM (Falck & Neyrinck 2015). Even in the 2D Lagrangian slice in Fig. 5, the void region obviously does pinch off into idealized convex voids (e.g. Icke & van de Weygaert 1991; Neyrinck 2014a).

4 VOID DETECTION AND PROPERTIES

ZOBOV first uses a Voronoi tessellation to get the density of each particle. After that, it uses each local density minimum as a seed

and groups other particles around it using the watershed algorithm, forming a 'zone', regions with a density and a ridge. These zones are combined into larger parent voids using essentially another application of the watershed algorithm, giving a hierarchy of subvoids.

In the default 'parameter-free algorithm output, the whole field is a single large supervoid with many levels of subvoids, which is difficult to use directly. We therefore required the zones added to a void to have core density less than $\bar{\rho}$, the mean density of the simulation. ZOBOV measures the statistical significance of voids, compared to a Poisson process. The probability that a void is real depends on the density contrast, defined as the ratio of the minimum density on the ridge separating the void from another void to the void's minimum density. To focus on voids with low discreteness effects, we analyse voids with significance larger than 3σ according to this density contrast criterion and measure their properties. We found about 7600, 6700, 3900, and 1400 voids for the four simulations. Consistently, with the results of Tikhonov et al. (2009), the number of voids decreases as the cutoff scale increases. Compared to Hamaus et al. (2014), our much higher mass resolution (compared to their sparse-sampling to better approximate a galaxy sample) allows much smaller voids to be detected in the matter field. We acknowledge that these smallest structures would likely not show up in a galaxy survey unless it was extremely deep. Even then, small voids may be smeared out by redshift-space distortions. However, some of these small (sub)voids would be in low-density regions, with smaller redshift-space distortions smearing them out. And also, we emphasize that many of these small void cores, at low sampling, would also likely be centres of larger, parent voids, that are not necessarily included in our pruned catalogue.

Comparing to Aragon-Calvo et al. (2010) and Aragon-Calvo & Szalay (2013), which considered the hierarchical structure of voids in different levels of smoothing, we do not explicitly take out the subvoids in each level of the hierarchy but use their effective sizes to characterize them. Apparently, larger voids show up in lower levels
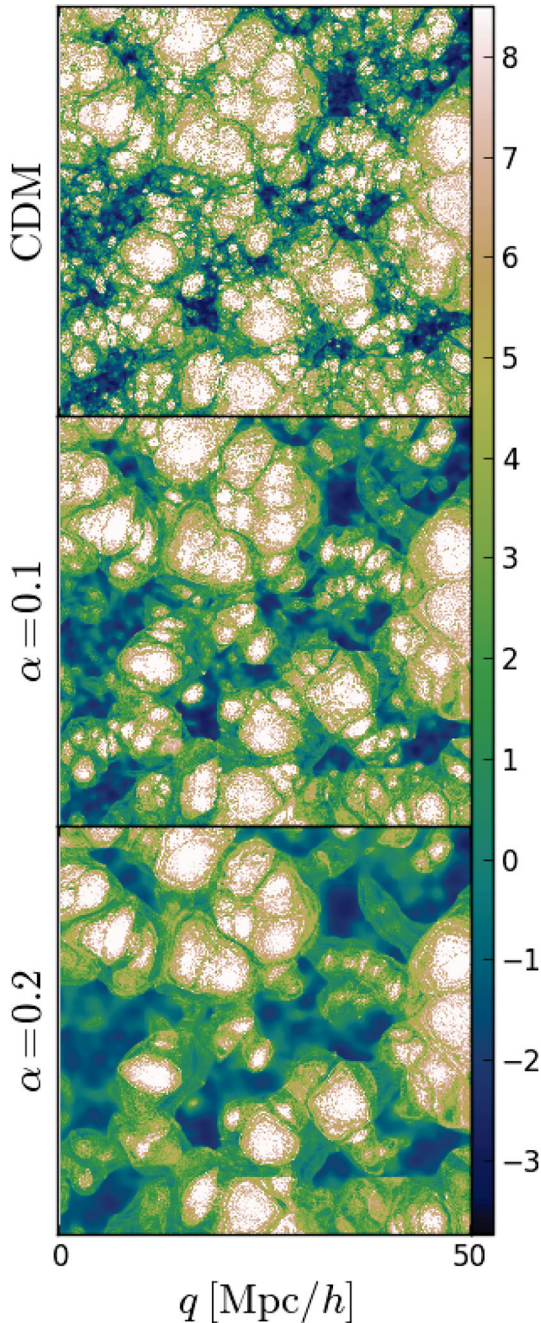
Figure 4. $z = 0$ Voronoi particle densities $\ln(1 + \delta)$ on a 2D Lagrangian sheet, with one particle per $0.2\,h^{-1}$ Mpc comoving Lagrangian pixel. Each panel shows a 2D, 256^2 slice, a quadrant of a full 512^2 slice.

Figure 5. Same as Fig. 4, with ORIGAMI morphologies added: black, red, and white contours separate void, wall, filament, and halo particle morphologies.

of the hierarchy tree. Fig. 6 shows distributions of void effective radius, r_{eff}, defined via $V_r = 4\pi/3 r_{\mathrm{eff}}^3$. The size of the voids in our simulations peaks roughly at $2\,h^{-1}$ Mpc, and shifts slightly outward at high α (moving to WDM). The abundances of voids around the interparticle spacing, $0.2\,h^{-1}$ Mpc, are very sensitive to discreteness noise. Thus, we truncate each plot on the left at twice the mean particle separation, at $\sim 0.4\,h^{-1}$ Mpc.

In the right tails ($r_{\mathrm{eff}} \gtrsim 3$ Mpc) of Fig. 6, there are more large voids in a WDM scenario, but not dramatically so. This may depend more on the void definition than the distribution of core densities, however, since the reported radius of a void obviously depends crucially on where its boundary is drawn. While at radius $\gtrsim 1$ Mpc,
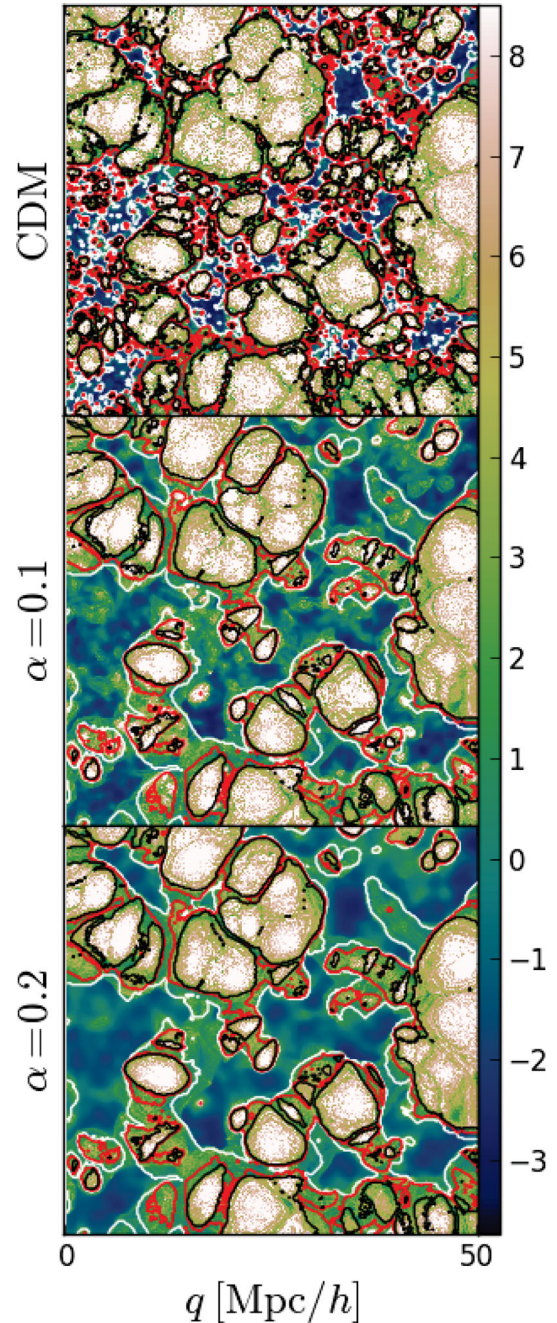
the abundance depression on the left and increasing at the right of the figure clearly shows the effect that sub-structures in larger voids have been suppressed. Fig. 7 shows the minimum 'core' Voronoi density distribution for voids and subvoids (in units of the mean density $\bar{\rho}$). It shows that the centres of voids become shallower in WDM. This is a simple physical effect: in WDM, the initial density PDF on the scale of the interparticle spacing is narrower than in CDM, because of the small-scale attenuation. This results in a narrower particle density distribution at $z = 0$, as shown in Section. 3. In particular, density minima, in the low-density tail, increase in density.
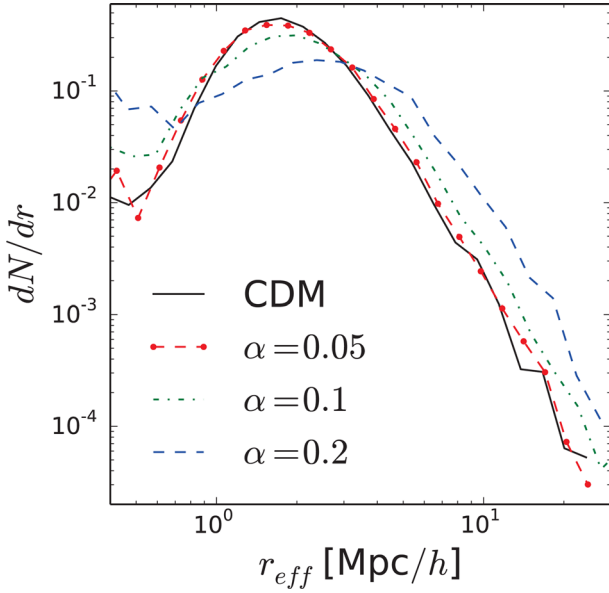
Figure 6. The void radius $r_{\rm eff}$ distribution for different DM models.

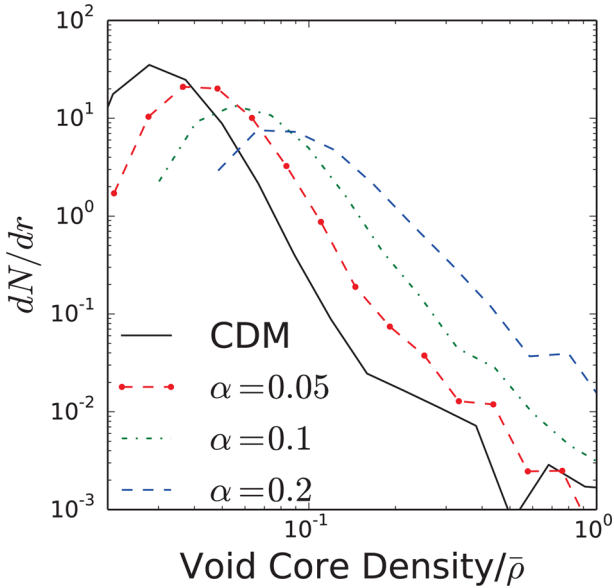**Figure 8.** The distribution of $r_{0.2}$ for different DM models.

Figure 7. The void core density distribution for different DM models.

5 DENSITY PROFILES

We take special interest in void density profiles, as they have been measured by several different authors recently (Clampitt & Jain 2014; Hamaus, Sutter & Wandelt 2014; Nadathur et al. 2014; Pisani et al. 2014; Ricciardelli, Quilis & Varela 2014). We show density profiles in Fig. 9. As found by Hamaus et al. (2014), smaller voids are, on average, deeper.

Our voids are mostly in the radius range 1–10 h^{-1} Mpc. We divide the voids into two bins of effective radius, 1–5 and 5–10 h^{-1} Mpc. We measure the density profiles starting from void centres using linear radial bins. For radial bin $[r, r + \Delta r)$, the density is simply $3N_r/4\pi[(r + \Delta r)^3 - r^3]$, where N_r is the number of particles detected in this bin. We investigate two definitions of the centre: (a) the actual density minimum of the void, as measured by the VTFE; and (b) the volume centroid of the void, defined as $\sum \boldsymbol{x}_i V_i / \sum V_i$, where $\boldsymbol{x}_i$ is the position of particle i belonging to the void, and V_i is
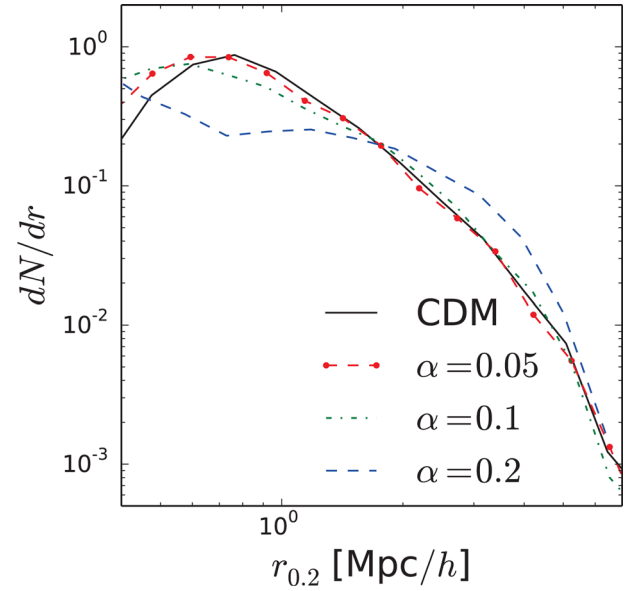
the Voronoi volume of that particle. The volume centroid would be easier to locate observationally than the density minimum. These profiles are further scaled by different radii r_s (i.e. $r_{\rm eff}$ or $r_{0.2}$) using linear interpolation. Note that for the profiles starting from the density minimum, the Voronoi tessellation always guarantees a particle in the centre, and hence a spike. We remove the central bin to remove such an artificial spike. Error bars of each data bin were measured using the standard deviation divided by $\sqrt{N}$, where N is the number of profiles stacked. The error bars shown in this paper are all 2σ errors.

Since the voids detected by ZOBOV are highly irregular in shape, ZOBOV's effective radius may not be the most meaningful radius measure in all cases. We visually check the voids and found that most of the irregularities are in the noisy edges of the voids. We therefore define a radius $r_{0.2}$ for voids such that at this point the average density encompassed is $0.2\bar{\rho}$, following Jennings, Li & Hu (2013). The distribution of $r_{0.2}$ is shown in Fig. 8. $r_{0.2}$ was typically from 0.5–3 h^{-1} Mpc. The distribution of voids of $r_{0.2} \gtrsim 0.5 \, h^{-1}$ Mpc shows similar features as does $r_{\rm eff}$ due to the small-scale suppression effect of WDM. Note that the number of small voids, with $r_{0.2} \lesssim 0.8 \, h^{-1}$ Mpc, is curiously higher in WDM than in CDM. For these poorly-resolved small voids, suppose WDM voids are simply shallower versions of CDM voids. The WDM voids will tend to have smaller $r_{0.2}$, since, starting from a higher density minimum, a sphere needs not go out as far to reach an enclosed density of $0.2\bar{\rho}$. Again we use the core particle as the centre, scaled the void profiles measured by shell bins by $r_{0.2}$, and stacked them, shown in Fig. 10. The central densities are quite similar across different voids. Note that $r_{0.2}$ is typically 2–3 times smaller than $r_{\rm eff}$. This is surprisingly large, but may be the effect of including the full, generally irregularly shaped, density ridges around voids. As discussed in Jennings et al. (2013), choosing a different definition of void size simply moves voids among radius bins, but does not change their total abundance.

The shallowing of the density profile in central bins is entirely unsurprising if the profiles are measured from density minima; this follows almost trivially from the increase in density minima. Less obvious is the behaviour of void profiles as measured from their volume centroids. The profile from the volume centroid is more
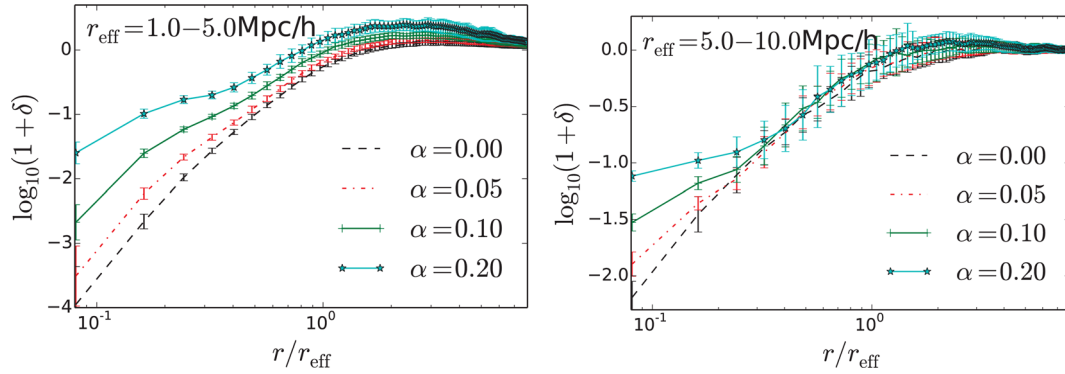
Figure 9. Void density profiles measured and scaled with r_{eff}. The origin is the density minimum of each void. The left-hand panel shows voids in the 1–5 h^{-1} Mpc radius bin; the right-hand panel shows results from 5–10 h^{-1} Mpc voids. Error bars show the 2σ error, dividing by $\sqrt{N}$, where N is the number of stacked voids.
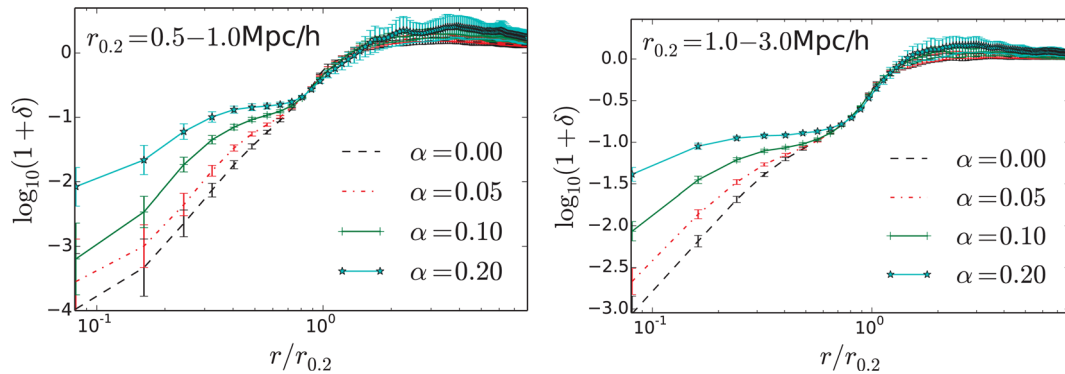

Figure 10. Void density profiles as in Fig. 9, except scaled with $r_{0.2}$. The left-hand panel shows the voids in the $0.5 - 1.0$ h^{-1} Mpc radius bin; the right-hand panel shows the 1.0–3.0 h^{-1} Mpc bin.
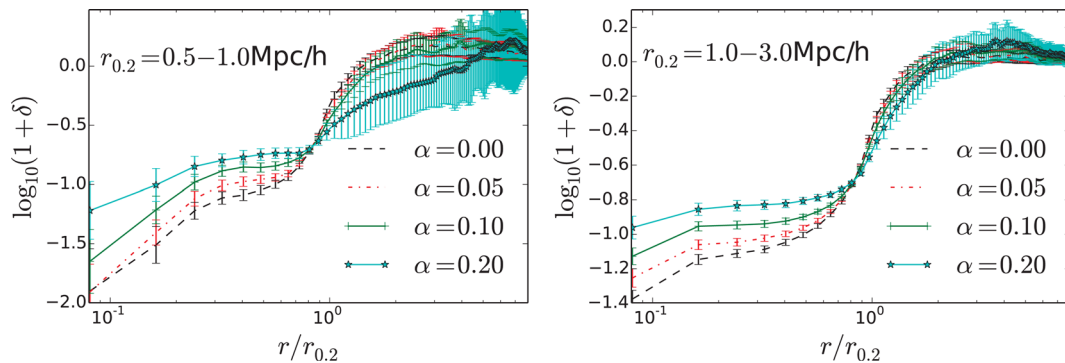

Figure 11. Void density profiles as in Fig. 10, except using void volume centroids as centres.

observationally relevant, because there is some hope of inferring it from a dense galaxy sample, while locating a 3D density minimum would be quite difficult. In Fig. 11, we show density profiles measured in the same way as before, except from the volume centroids using the Voronoi volumes of all particles reported in the ZOBOV void. These profiles are scaled by $r_{0.2}$ and stacked in the same radius bins as in the previous case. As previously, we tried to use r_{eff} to scale and stack, but in highly noisy profiles. The reason is the same: the shapes of the voids become irregular when their sizes are small, and there is some randomness in whether part of a density ridge is included or not, so the ZOBOV effective radius can be noisy.

Either scaling the profile with $r_{0.2}$ or r_{eff}, the density profiles show some universalities – the central part of the profile is relatively

stable. For different DM settings, the centre part of the profiles is clearly different. While the profiles when scaling by $r_{0.2}$ are less noisy than those scaled by r_{eff}, the profiles' shapes are similar in both cases. It is reassuring that the results hold whether the volume centroid or the density minimum is used to measure the density profile.

In most previous profile studies, people use the effective radius r_{eff} to scale the density profile and get universal profiles – a relatively flat central plateau, a sharp edge and a compensated wall, tending to unity faraway. We argue that using $r_{0.2}$, the radius at which the mean enclosed density reaches 0.2, as a scaling constant to find small void profiles is better. The void wall radius deviates from r_{eff} significantly with non-spherical shapes, while $r_{0.2}$ characterizes every void in the

context of a spherical-evolution model. If the voids are self-similar, as stated in Nadathur et al. (2014), $r_{0.2}$ surely returns more consistent profiles. This is indeed shown in Figs 10 and 11. Since the slope of profiles is apparently the largest at $r \approx r_{0.2}$, a lensing measurement would be most sensitive if using this definition.

6 CONCLUSION AND DISCUSSION

We measure statistics and density profiles of voids in different DM settings, namely CDM, and WDM with characteristic scales $\alpha = 0.05$, 0.1 and 0.2 h^{-1} Mpc. In summary, the voids in WDM are shallower. WDM voids also tend to be larger, although this effect depends somewhat on the void definition. The number of statistically significant voids is also smaller in WDM simulations. The main question this paper poses is whether void density profiles can be used to detect WDM, or some other process that attenuates initial small-scale power. Our answer is yes, in principle.

One advantage of using voids rather than high-density regions is that the structure of voids is much less sensitive to baryonic physics than in high-density regions. This is because matter in voids undergoes no stream-crossing on cosmological scales (e.g. Falck & Neyrinck 2015). Substantial differences between DM and baryonic physics are only expected when streams collide; in collisionless DM, the streams pass through each other, while streams of gas collide, e.g. forming shocks.

However, it is quite difficult to constrain matter density profiles observationally, even if the voids themselves can be located using galaxies or other tracers, which becomes tricky at small radius because of issues such as redshift-space distortions. Lensing could be used to constrain density profiles, as shown in Clampitt & Jain (2014). However, lensing is only sensitive to the gradient of the surface density, which becomes zero at the very centre of the void. Fortunately, our results do show a difference in the density gradient in different WDM scenarios. Another possible probe is the integrated Sachs–Wolfe effect (e.g. Granett, Neyrinck & Szapudi 2008), usefully sensitive to the potential, although that measure is difficult to detect for small voids because of the dominant primordial CMB. But there are other probes of the potential through voids, such as in fluctuations in the cosmic expansion rate as measured with supernovae. Another aspect of voids that we did not measure, but would also be sensitive to matter density profiles, is the velocity field within voids; perhaps very faint tracers such as absorption lines can be used to constrain these (e.g. Tejos et al. 2012). Another possible direction to constrain WDM is through the properties of filaments and perhaps walls in WDM, which we quantitatively showed become more prominent; however, we leave a detailed study of their properties such as density profiles to future work.

ACKNOWLEDGEMENTS

REFERENCES

Abel T., Hahn O., Kaehler R., 2012, MNRAS, 427, 61
Ackermann M. et al., 2014, Phys. Rev. D, 89, 042001
Agnese R. et al., 2013, Phys. Rev. Lett., 111, 251301
Akerib D. S. et al., 2014, Phys. Rev. Lett., 112, 091303
Angulo R. E., Hahn O., Abel T., 2013, MNRAS, 434, 3337
Aprile E., 2013, in Cline D., ed., Sources and Detection of Dark Matter and Dark Energy in the Universe. Springer, p. 93
Aragon-Calvo M. A., Szalay A. S., 2013, MNRAS, 428, 3409
Aragon-Calvo M. A., van de Weygaert R., Araya-Melo P. A., Platen E., Szalay A. S., 2010, MNRAS, 404, L89
Bernardeau F., 1994, ApJ, 427, 51
Bertone G., Hooper D., Silk J., 2005, Phys. Rep., 405, 279
Bode P., Ostriker J. P., Turok N., 2001, ApJ, 556, 93
Boyarsky A., Lesgourgues J., Ruchayskiy O., Viel M., 2009, J. Cosmol. Astropart. Phys., 2009, 012
Cai Y.-C., Padilla N., Li B., 2014, preprint (arXiv:1410.1510)
Carron J., 2011, ApJ, 738, 86
Carron J., Neyrinck M. C., 2012, ApJ, 750, 28
Clampitt J., Jain B., 2014, preprint (arXiv:e-prints)
Clampitt J., Cai Y.-C., Li B., 2013, MNRAS, 431, 749
Falck B., Neyrinck M. C., 2015, MNRAS, in press
Falck B. L., Neyrinck M. C., Szalay A. S., 2012, ApJ, 754, 126
Frenk C. S., White S. D., 2012, Ann. Phys., Lpz., 524, 507
Gao L., Theuns T., 2007, Science, 317, 1527
Gao L., Theuns T., Springel V., 2014, preprint (arXiv:e-prints)
Ghigna S., Moore B., Governato F., Lake G., Quinn T., Stadel J., 2000, ApJ, 544, 616
Granett B. R., Neyrinck M. C., Szapudi I., 2008, ApJ, 683, L99
Hamaus N., Sutter P. M., Wandelt B. D., 2014, Phys. Rev. Lett., 112, 251302
Hill J. C. et al., 2014, preprint (arXiv:e-prints)
Hoeft M., Yepes G., Gottlöber S., Springel V., 2006, MNRAS, 371, 401
Icke V., 1984, MNRAS, 206, 1p
Icke V., van de Weygaert R., 1991, QJRAS, 32, 85
Jennings E., Li Y., Hu W., 2013, MNRAS, 434, 2167
Kamionkowski M., Verde L., Jimenez R., 2009, J. Cosmol. Astropart. Phys., 2009, 010
Lavaux G., Wandelt B. D., 2012, ApJ, 754, 109
Lewis A., Challinor A., Lasenby A., 2000, ApJ, 538, 473
Li B., Zhao G.-B., Koyama K., 2012, MNRAS, 421, 3481
Mateo M. L., 1998, ARA&A, 36, 435
Miranda M., Macciò A. V., 2007, MNRAS, 382, 1225
Moore B., Ghigna S., Governato F., Lake G., Quinn T., Stadel J., Tozzi P., 1999a, ApJ, 524, L19
Moore B., Quinn T., Governato F., Stadel J., Lake G., 1999b, MNRAS, 310, 1147
Moroi T., Murayama H., Yamaguchi M., 1993, Phys. Lett. B, 303, 289
Nadathur S., Hotchkiss S., Diego J. M., Iliev I. T., Gottlöber S., Watson W. A., Yepes G., 2014, preprint (arXiv:e-prints)
Navarro J. F., Frenk C. S., White S. D. M., 1997, ApJ, 490, 493
Neyrinck M. C., 2008, MNRAS, 386, 2101
Neyrinck M. C., 2013, MNRAS, 428, 141
Neyrinck M. C., 2014a, Proc. 6th International Meeting on Origami in Science, Mathematics, and Education, sumbitted
Neyrinck M. C., 2014b, preprint (arXiv:e-prints)
Neyrinck M. C., 2014c, preprint (arXiv:e-prints)
Peebles P. J. E., 1980, The Large-Scale Structure of the Universe. Princeton Univ. Press, Princeton, NJ
Peebles P., 2001, ApJ, 557, 495
Pisani A., Lavaux G., Sutter P. M., Wandelt B. D., 2014, MNRAS, 443, 3238
Protogeros Z. A. M., Scherrer R. J., 1997, MNRAS, 284, 425

Reed D. S., Schneider A., Smith R. E., Potter D., Stadel J., Moore B., 2014, preprint (arXiv:e-prints)

Ricciardelli E., Quilis V., Varela J., 2014, MNRAS, 440, 601

Ryden B. S., 1995, ApJ, 452, 25

Schaap W. E., van de Weygaert R., 2000, A&A, 363, L29

Schaeffer R., Silk J., 1988, ApJ, 332, 1

Schneider A., Smith R. E., Macciò A. V., Moore B., 2012, MNRAS, 424, 684

Springel V., 2005, MNRAS, 364, 1105

Tejos N., Morris S. L., Crighton N. H. M., Theuns T., Altay G., Finn C. W., 2012, MNRAS, 425, 245

Tikhonov A. V., Gottlöber S., Yepes G., Hoffman Y., 2009, MNRAS, 399, 1611

van de Weygaert R., Schaap W., 2009, in Martínez V. J., Saar E., Martínez-González E., Pons-Bordería M.-J., eds, Lecture Notes in Physics, Vol. 665, Data Analysis in Cosmology. Springer-Verlag, Berlin, p. 291

Viel M., Becker G. D., Bolton J. S., Haehnelt M. G., 2013, Phys. Rev. D, 88, 043502

Wang J., White S. D. M., 2007, MNRAS, 380, 93

Zel'dovich Y. B., 1970, A&A, 5, 84

This paper has been typeset from a TEX/LATEX file prepared by the author.